

RTM of a distributed acoustic sensing VSP at the CaMI Field Research Station, Newell County, Alberta, Canada

Jorge E. Monsegny, Daniel Trad and Don C. Lawton

ABSTRACT

We applied a reverse time migration (RTM) algorithm to distributed acoustic sensing (DAS) data from a walkaway vertical seismic profiling (VSP) acquisition at the CaMI Field Research Station at Newell County, Alberta, Canada. The RTM algorithm used a system of coupled first degree differential equations for pressure, vertical and horizontal particle velocities. As DAS data measurements are usually strain rate, we transformed them to vertical particle velocity before the RTM algorithm back propagated them. We tested the techniques of Daley et al. (2016) and Bóna et al. (2017) to do this transformation. We also tested the RTM with the original DAS data. Apart from a polarity reversal, there were no important differences between the different RTM tests. In addition, we migrated geophone data from the same VSP acquisition for comparison and found a similar imaging quality.

INTRODUCTION

The University of Calgary, in association with CMC Research institutes Inc., have a facility in Newell County, Alberta, called Containment and Monitoring Institute (CaMI) Field Research Station (FRS), where new technologies for carbon capture and storage (CCS) monitoring are being developed (Lawton et al., 2015). The plan is to inject up to 400 tonnes of CO₂ per year over 5 years inside water-saturated sandstones within the Upper Cretaceous formations, with overlying shales and mixed sand/shale sequences forming the cap rocks (Macquet et al., 2019).

The stored CO₂ perturbs the effective elastic properties of the surrounding rocks (P-wave velocity, S-wave velocity and density) (Macquet and Lawton, 2017). Therefore, a facility of this kind requires frequent monitoring of these properties changes to monitor the location of CO₂ injection, the volumetric extension of CO₂ migration and to detect possible CO₂ leaks (Lumley et al., 2010). For this reason, at CaMI-FRS, multicomponent geophones and state-of-the-art distributed acoustic sensing (DAS), that uses fibre optic cables (Daley et al., 2013), are permanently installed in two wells, a trench and an area around the injection facilities (Lawton et al., 2017). Figure 1 shows the layout of the DAS monitoring facilities.

Distributed acoustic sensing is a technology derived from the optical time domain interferometry that uses optical fibre as a distributed sensing element to measure strain (Hartog, 2018). Basically, a short but highly coherent light pulse is sent through the fibre and the Rayleigh back scattered light that returns is analyzed to detect strain changes along the fibre. One popular approach uses interferometry to obtain the phase difference between the back scattered light from two fibre sections separated by a gauge length (Juškaitis et al., 1994; Kwon et al., 1999; Masoudi et al., 2013). This phase difference can be related to the fibre strain using the phase-strain model of Sirkis and Henry W. Haslach (1991). It is important to realize that the measured strain is due to fibre length changes along all the

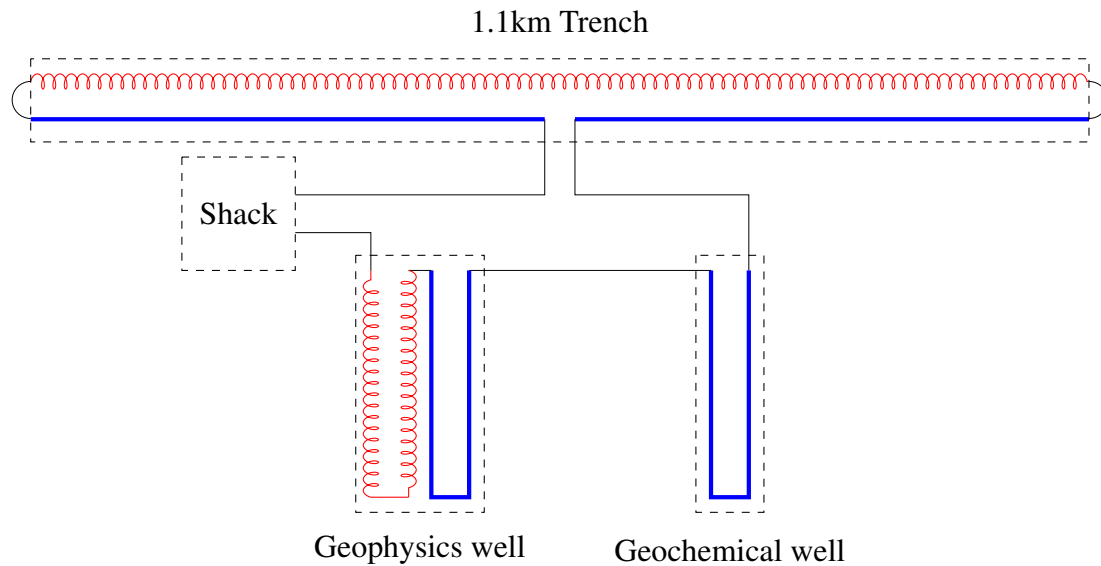


FIG. 1. Permanent DAS facilities installed in CaMI-FRS trench and wells (Lawton et al., 2017). Red coil is helical fibre and blue thick line is straight fibre. The DAS interrogator and all the associated equipment are located inside the Shack.

gauge length (around 10 metres in many implementations) and not on a single fibre point. It is also important to mention that some DAS implementations output strain rate instead of simply strain (Hartog, 2018).

VSP data can be imaged using a variety of techniques like VSP-CDP transform, Kirchhoff migration, RTM, beam migration, image point transform and interferometric methods. Dillon and Thomson (1984) used ray tracing to map walkaway VSP data from its local coordinate system to the common midpoint (CMP) coordinate system by moving each sample laterally to its presumed reflection point. Although this mapping creates a familiar subsurface image, it assumes horizontal layers precluding its application to more complex geologies. Wiggins et al. (1986) related the VSP to CDP transform to the VSP migration by using the former as a step towards finding the velocity model for the second. Dillon (1988) tested complex synthetic models and finds that VSP to CDP mapping misplaces dipping reflectors.

The first attempts to migrate walkaway VSP data used Kirchhoff migration (Keho, 1984; Dillon, 1985). Ranganayaki and Moeckel (1987) used a simplified version of the Kirchhoff summation that is not dip-limited for migrating deviated and shear wave VSP data sets. Lou et al. (2009) proposed a method to choose an appropriate migration aperture and a smoothing least squares migration operator to eliminate artifacts in Kirchhoff migration of VSP data. Zhao and Jin (2015) incorporated structure-dip information to the Kirchhoff migration of VSP data. The result allows the imaging of dip structures far from the well and less ambiguity in the imaging results.

Chang and McMechan (1986) proposed a RTM for VSP data with the excitation time imaging condition which is a generalization of Claerbout's imaging condition. Whitmore and Lines (1986) used RTM to image salt dome flanks from VSP data. They first find

the velocity model using linear tomography and then apply a scalar imaging condition. Hou et al. (2000) used a hybrid scheme with finite differences for the shot gathers back propagation and ray tracing for the forward propagation. Their aim was to include multiples in the VSP migration. Chon et al. (2003) compared scalar and elastic RTM of VSP data finding a superior quality of the elastic migration. Leung et al. (2013) separated the VSP data in up- and down-going parts and obtained images with improved image coverage. Xue and Liu (2017) used the Hilbert transform and wavefield decomposition imaging condition to eliminate the noise caused by the direct wave in the RTM of VSP data. This solution avoids the use of the Laplacian filtering to suppress the low frequency noise associated with RTM. Liu et al. (2018) also suppressed RTM low frequency noise in VSP data by introducing an eight-direction wavefield decomposition imaging approach.

Cosma and Heikkinen (1996) introduced the image point transform as a means to image VSP data. This transform is based on the Radon transform, with the difference that it stacks traces along straight paths enhancing weak reflections and giving a direct measure of reflector strength. Cosma et al. (2010) extended the image point transform to a 3D VSP migration that enhances reflectors and suppresses other events like multiples and noise.

Yu and Schuster (2004) used crosscorrelation to perform a seismic interferometry migration of VSP data. This approach increased the illuminated zone compared to classic VSP migration. He et al. (2007) also used interferometry to migrate free surface multiples in VSP data. Apart from a larger imaging area, the method is less sensitive to velocity errors than other methods for migration with multiples. Lomas et al. (2019) reduced the artifacts created in VSP imaging due to the improper handling of internal multiples by using Marchenko methods that are able to redatum the receivers at an arbitrary point inside the subsurface of the Earth.

Wang et al. (2011) perform a RTM of time-lapse walkaway VSP data for monitoring CO₂ injection. They conclude that this RTM can reveal reservoir changes due to CO₂ injection and migration. Chavarria et al. (2019) also uses RTM to monitor CO₂ injection, but they use VSP DAS data that provides high survey repeatability and improved resolution.

In this report we perform an acoustic RTM of the walkaway VSP DAS data from the CaMI site. The report plan is the following. We first explain the finite difference scheme we used for modelling and migration, then we mention the imaging condition we used. Following that, we explain how we transformed strain rate, what DAS measures, to particle velocity, that is what our RTM migrates. Next, we do a synthetic modelling and migration experiment trying to emulate all conditions of the real VSP DAS data at CaMI site. Finally, we apply the RTM algorithm to the real data and show the migration results.

METHODS

Acoustic finite differences

We use the finite difference system defined in Liang et al. (2018). This is a staggered system in pressure P , vertical v_z and horizontal particle velocity v_x with density ρ and first Lamé parameter λ :

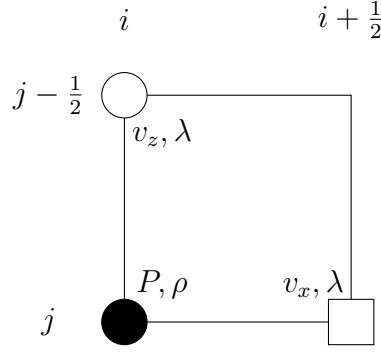


FIG. 2. Location of the finite difference wavefields in the staggered grid. Pressure P and density ρ are at integer coordinates (i, j) , vertical particle velocity v_z is at coordinates $(i, j - 1/2)$, horizontal particle velocity v_x is at $(i + 1/2, j)$ and Lamé parameter λ is defined at both $(i, j - 1/2)$ and $(i + 1/2, j)$

$$\begin{aligned}
 \frac{\partial P}{\partial t} &= \lambda \left(\frac{\partial v_x}{\partial x} + \frac{\partial v_z}{\partial z} \right) + s \\
 \frac{\partial v_x}{\partial t} &= \frac{1}{\rho} \frac{\partial P}{\partial x} \\
 \frac{\partial v_z}{\partial t} &= \frac{1}{\rho} \frac{\partial P}{\partial z}
 \end{aligned} \tag{1}$$

where the source s is injected in the pressure equation. Figure 2 shows the location of each finite difference wavefield in the staggered grid. Pressure P and density ρ are at integer coordinates (i, j) , vertical particle velocity v_z is at coordinates $(i, j - 1/2)$, horizontal particle velocity v_x is at $(i + 1/2, j)$ and Lamé parameter λ is defined at both $(i, j - 1/2)$ and $(i + 1/2, j)$.

We adopt a split perfectly matched layer (SPML) scheme to absorb reflections from the domain limits. The SPML divides the equation for pressure P in P_x and P_z components (Collino and Tsogka, 2001):

$$\begin{aligned}
 P &= P_x + P_z \\
 \frac{\partial P_x}{\partial t} + d(x)P_x &= \lambda \frac{\partial v_x}{\partial x} + \frac{s}{2} \\
 \frac{\partial P_z}{\partial t} + d(z)P_z &= \lambda \frac{\partial v_z}{\partial z} + \frac{s}{2} \\
 \frac{\partial v_x}{\partial t} + d(x)P_x &= \frac{1}{\rho} \frac{\partial P}{\partial x} \\
 \frac{\partial v_z}{\partial t} + d(z)P_z &= \frac{1}{\rho} \frac{\partial P}{\partial z},
 \end{aligned} \tag{2}$$

using coefficients $d(u)$ for $u = x, z$ inside a SPML boundary of thickness L where u is the distance to the original domain border. These coefficients are calculated according to:

$$d(u) = d_0 \frac{u^2}{L^2} \quad \text{with} \quad d_0 = -\frac{3v}{2L} \ln(R), \quad (3)$$

where $R = 10^{-5}$ and v is the highest P-wave propagation velocity. In contrast, inside the domain, $d(u) = 1$.

Reverse time migration

We implement the standard RTM algorithm (Baysal et al., 1983) for walkaway VSP DAS data. Specifically, the source wavelet is propagated from the source points on the surface while the recorded data is back propagated at several receiver positions along the vertical fibre. We use the imaging condition for vertical particle velocity v_z as the straight DAS fibre is mainly sensitive in the axial direction (Hartog, 2018), and in vertical VSP this direction coincides with the z axis. The normalized imaging condition is the following:

$$I(x, z) = \frac{\int_0^T v_z(x, z) \hat{v}_z(x, z) dt}{\int_0^T v_z(x, z)^2 dt}, \quad (4)$$

where the hat symbol " $\hat{}$ " indicates back propagation, the denominator term is used to correct the source illumination and T is the maximum time recorded.

Strain rate to particle velocity transformation

A vertical DAS measures vertical strain rate $f = \frac{\partial \epsilon_z}{\partial t}$ where ϵ_z is the strain along the z axis. In order to apply the imaging condition of equation 4 we have to transform this strain rate to vertical particle velocity. We test two approaches. The first one is from Daley et al. (2016):

$$v_z(z) = -c(z) \int f(z) dt, \quad (5)$$

where $f(z)$ is the fibre response and $c(z)$ is the apparent particle velocity along the well measured from the first arrivals moveout. The second approach is from Bóna et al. (2017):

$$v_z(k_z) = f(k_z) \frac{-ik_z}{(1 - e^{ik_z L})(1 - e^{ik_z G}) + \gamma}, \quad (6)$$

where L is the pulse length, G is the gauge length and γ is a small constant used to avoid division by zero. This filtering operation is performed in the wavenumber domain k_z .

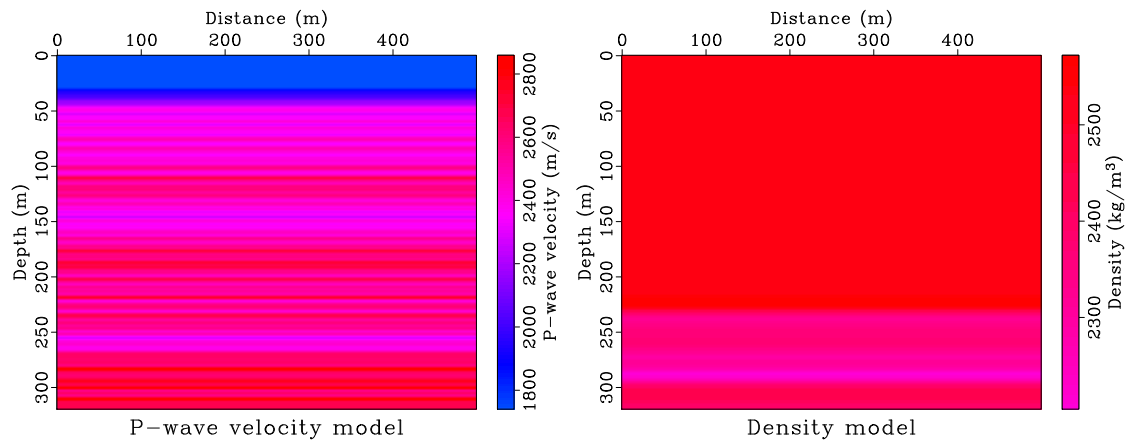


FIG. 3. P-wave and density models of CaMI site with a 10m vertical smoothing.

The opposite transformation, from vertical particle velocity v_z to vertical strain rate, is needed during modelling. Noticing that v_z is the time derivative of vertical particle displacement u_z we can take its spatial derivative along the z axis to get the corresponding vertical strain rate:

$$f = \frac{\partial \epsilon_z}{\partial t} = \frac{\partial}{\partial t} \left(\frac{\partial u_z}{\partial z} \right) = \frac{\partial}{\partial z} \left(\frac{\partial u_z}{\partial t} \right) = \frac{\partial v_z}{\partial z} \quad (7)$$

SYNTHETIC EXPERIMENT

We perform a synthetic experiment that approximates the data from the walkaway VSP DAS in the observation well 2 at the CaMI site. Figure 3 shows the P-wave velocity and density models used in this synthetic experiment. We apply a 10m vertical smoothing to both of them to make the wave propagation simulation stable.

The source wavelet is chosen by inspecting the amplitude spectrum of the real VSP DAS data from CaMI. The left part of Figure 4 displays this spectrum with frequencies centred around 100Hz. The right part of the same figure shows the minimum phase wavelet with central frequency equal to 100Hz that was used in the data modelling and migration.

We model 17 shots located more or less evenly spaced at the surface in a straight line close to the well. The original data was sampled every 0.25m and goes from the surface to a depth of 320.25m. We are going to model receivers along the DAS fibre from 84m to 317m every 1m to match a zone with good signal in the real data and to have an affordable data size. Figure 5 shows the real VSP DAS data after processing (Gordon, 2019) and the DAS modelled data.

In the synthetic modelling we use the acoustic finite difference system of equation 1 to record the vertical particle velocity v_z at each receiver location. Then we transform these traces to strain rate using equation 7. It is important to point out that we did this

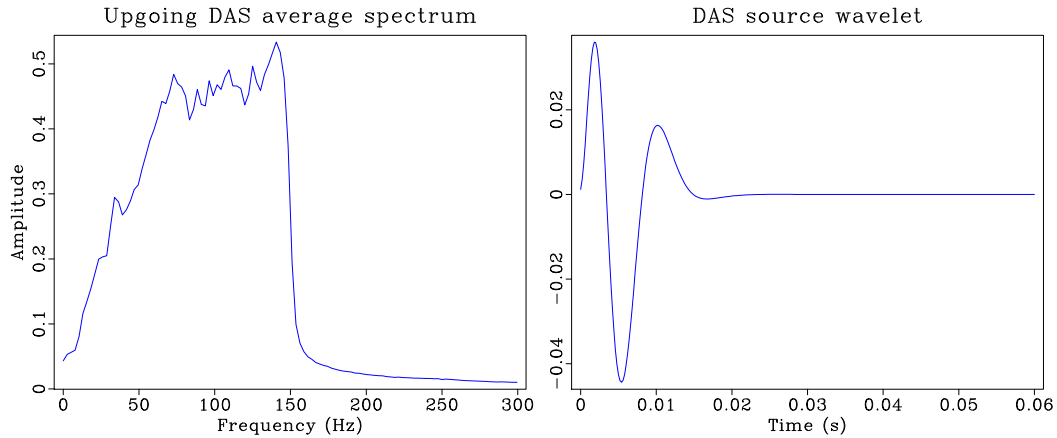


FIG. 4. Left is the average spectrum of the upgoing DAS VSP data. Right is the minimum phase source wavelet used in the numerical experiments. It has a central frequency of 100Hz because the real data is centred around this frequency.

transformation only to compare real and modelled DAS data. The RTM is done directly using the modelled v_z . Figure 5 shows the real and the modelled VSP DAS data.

Figure 6 shows the RTM result using the imaging condition of equation 4 without, left, and with, right, a Laplacian filter applied to suppress the RTM low frequency noise. The red crosses are the source positions and the green vertical line indicates the VSP DAS segment used. It should be noticed that the source and receiver noise are very strong even after trying to suppress them with the normalized imaging condition (Equation 4) and that the events are mainly due to the discontinuities in the P-wave velocity model of Figure 3.

FIELD DATA RTM

The real data set is a walkaway VSP DAS composed of 17 shot gathers with spacing between 10m and 30m. The source was an IVI EnviroVibe with a linear sweep from 10Hz to 150Hz. There was a vertical DAS fibre with gauge length equal to 10m and traces from the surface to 320.25m deep every 0.25m (Gordon, 2019). There were also 24 multicomponent geophones from 191.25m to 306.25m every 5m inside the well.

Processing for both DAS and geophone data sets included geometry and first break picking, wavefield separation through median filtering and F-K filtering, gain for spherical spreading and transmission loss, and deconvolution of upgoing wavefield (Gordon, 2019). As mentioned previously, we select the DAS data from 84m to 317m every 1m because this interval is less noisy and its size is adequate. Figure 7 shows the processed upgoing DAS and vertical geophone component data sets.

For the migration of the field VSP data we use the same P-wave velocity, density and source wavelet of figures 3 and 4. Before feeding the RTM algorithm with the DAS data we transform it to vertical particle velocity using equations 5 and 6. For equation 5 we measured the direct wave velocity at the shot gather with the closest source to the well and found a constant apparent velocity of $c = 3500\text{m/s}$. For equation 6 we use a gauge length $G = 10\text{m}$ and ignore the pulse length term. We also perform the RTM without transforming

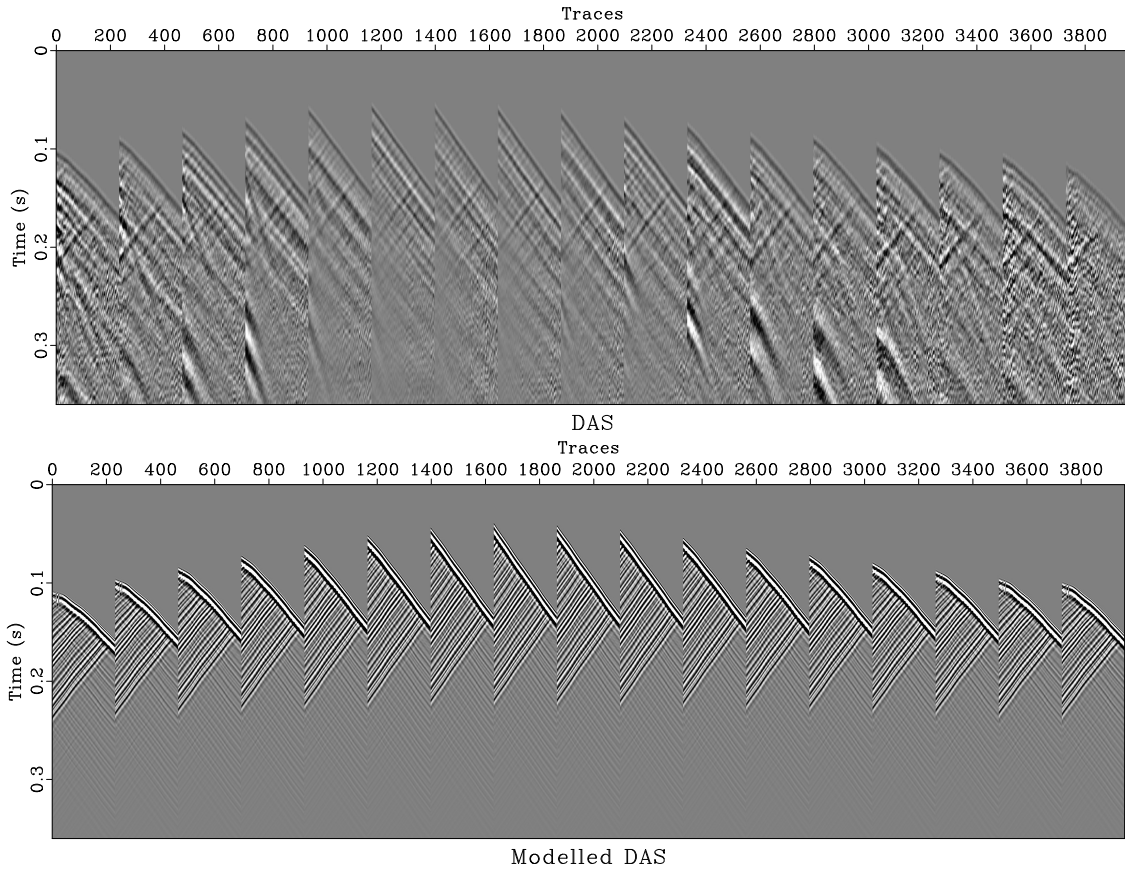


FIG. 5. Top is the real data from the walkaway VSP DAS after processing Gordon (2019). Bottom is the corresponding modelled data. Both data sets are composed of 17 shots and have receivers along the DAS fibre from 84m to 317m every 1m.

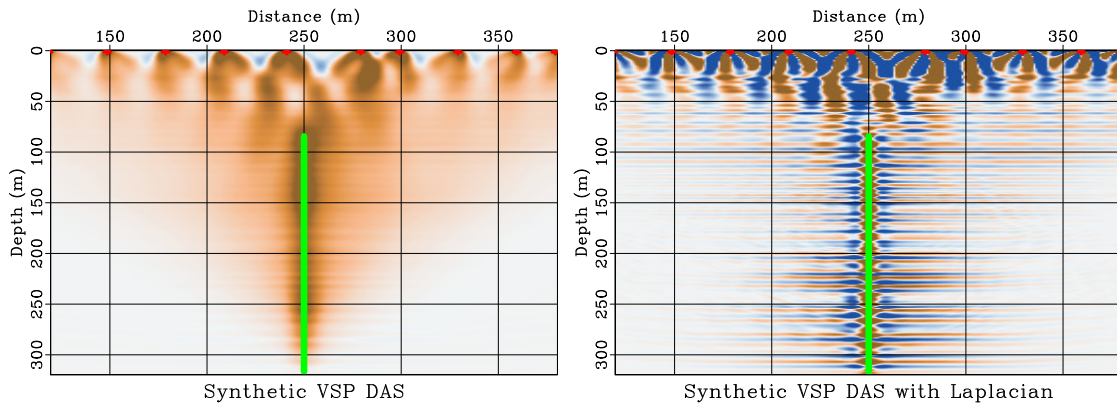


FIG. 6. RTM of the synthetic VSP DAS data using the imaging condition of equation 4. A Laplacian filter is applied to the right figure. Red crosses are source locations and the vertical green line indicates the VSP DAS segment used.

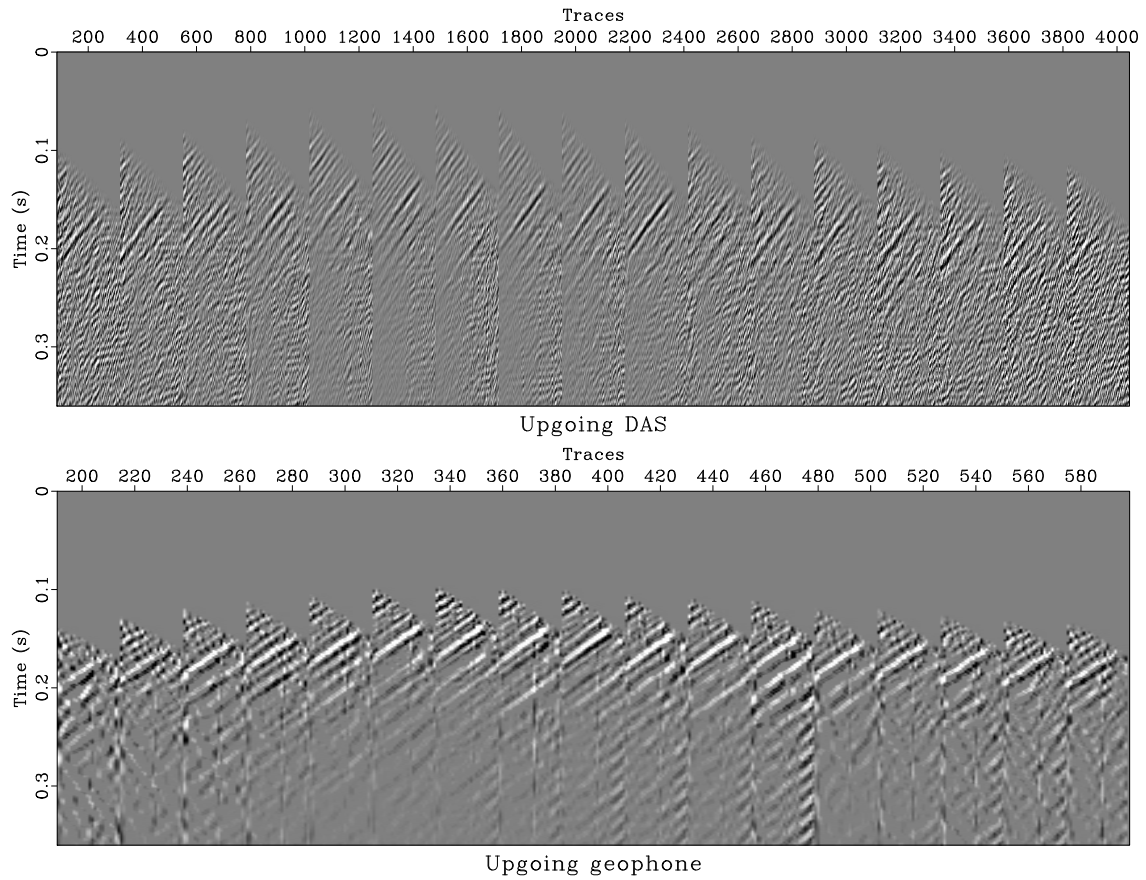


FIG. 7. Top is the real VSP DAS upgoing component from 84m to 317m every 1m while bottom is the real VSP geophone vertical particle velocity upgoing component from 191m to 306m every 5m (Gordon, 2019).

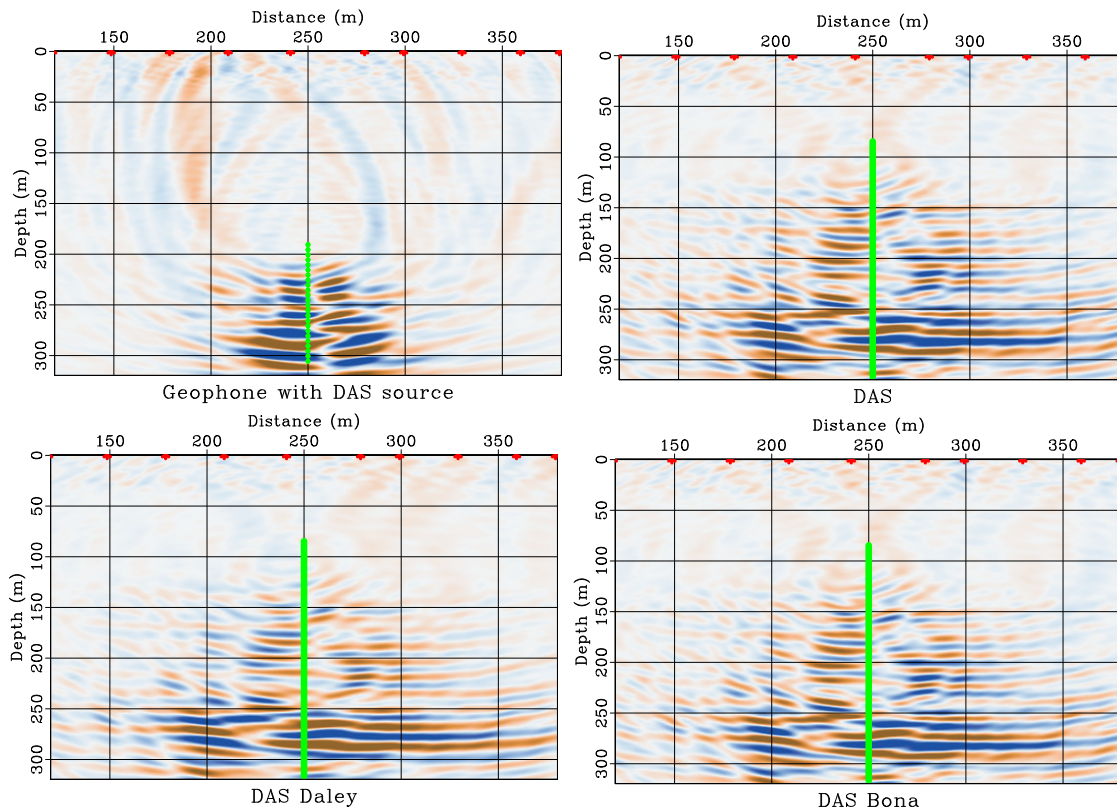


FIG. 8. Top row left is the RTM from 24 vertical geophones located inside the well (green dots) between 191m and 306m deep every 5m and 17 source positions placed at the surface (red crosses). Top row right is the RTM from a DAS fibre located in the well (green line) between 85m and 317m deep. It uses the same sources of the previous figure. The DAS data was not transformed before being used in the RTM, i.e. strain rate was back propagated by the migration algorithm. Bottom left uses the same DAS and sources configuration but transforms the strain rate measurements into particle velocity using the technique of Daley et al. (2016). Bottom right also transforms DAS measurements to particle velocity but it uses the technique of Bóna et al. (2017). Laplacian filtering was not applied to any figure because it did not produce any noticeable effect.

the DAS data and with the geophone data. Figure 8 shows the migration results.

In Figure 8 we show the geophone RTM using the wavelet derived from DAS data spectrum. However, the geophone data has a slightly different spectrum as shown in Figure 9. This spectrum is centred around 60Hz. We also used different receiver spreads for geophone and DAS data. In order to be fair, we perform additional experiments: A geophone RTM using the minimum phase wavelet of Figure 9 and the DAS migrations with the same receiver spread used by the geophone data. The results are shown in Figure 10.

DISCUSSION

The first thing to notice is the difference between the RTM using synthetic data and the RTM using real data. The filtering of low frequency noise generated by the RTM did not make a noticeable effect in the RTM with real data (figures 8 and 10). On the other hand, this filtering was essential for the RTM with synthetic data as Figure 6 shows. One probable reason is that in the synthetic experiment we used the whole traces, including the strong first arrivals, while in the real experiments we back propagated only the up-going

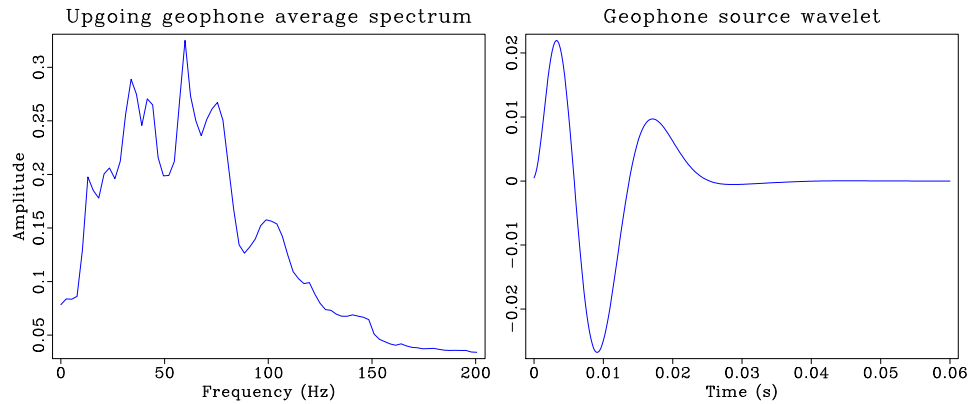


FIG. 9. Upgoing VSP geophone average amplitude spectrum and the geophone modelling minimum phase wavelet with central frequency equal to 60Hz.

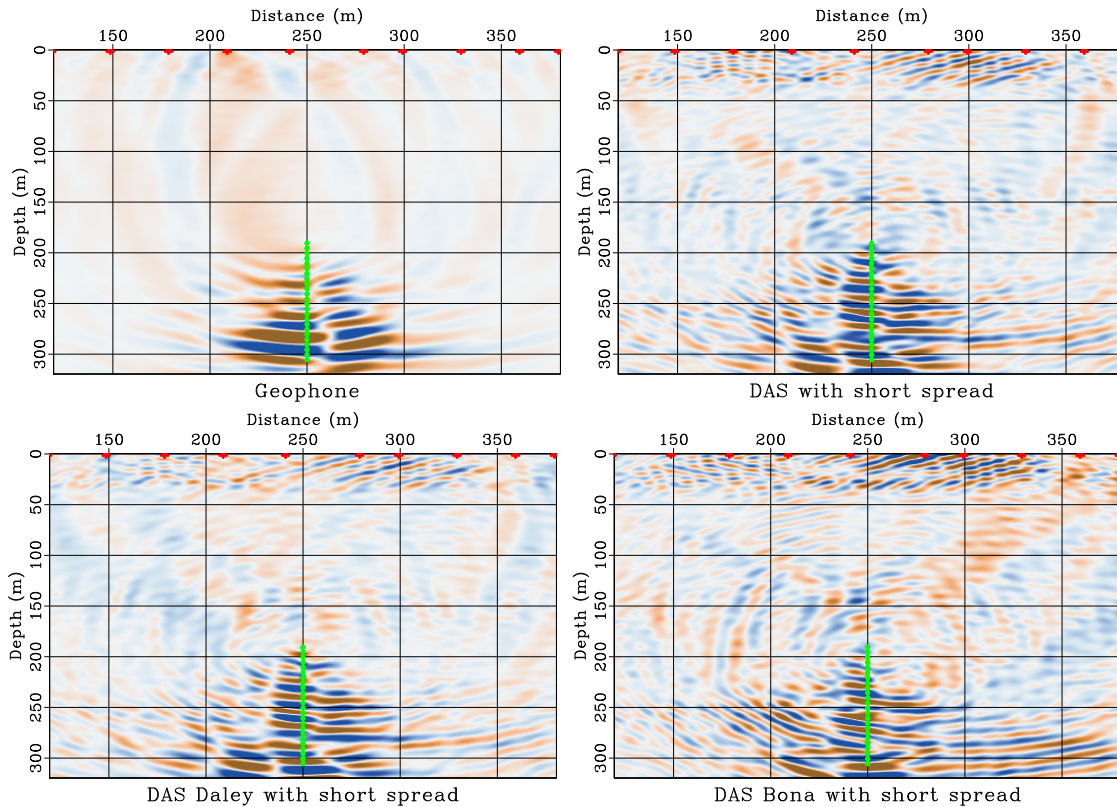


FIG. 10. Top left is the walkaway VSP geophone RTM with a 60Hz minimum phase source wavelet. The other three RTM sections use a 100Hz source wavelet but their receiver spreads have been decimated to match the geophone receiver spread. Top right is the untransformed DAS RTM. Bottom left is the RTM of DAS data transformed using the technique of Daley et al. (2016) while bottom right uses the technique of Bóna et al. (2017).

part of the data.

The noise associated with sources and receivers was very pronounced in the synthetic data RTM. In fact, their amplitudes were so high that the RTM of Figure 6 required a 90 percent amplitude clipping to be able to show the reflectors. On the other hand, real data RTM case had low source noise and almost no receiver noise so the amplitudes of figures 8 were all clipped to only 98 percent. The explanation could be again related to the use of up-going traces in the real experiments. We avoid the use of the first arrivals that produce strong but spurious events in the RTM section.

Other aspect to notice about the RTM results is that in the synthetic data RTM the imaged zone has an inverted triangle shape with the wide part along the surface and the apex at the deepest part of the fibre (Figure 6). In contrast, all the real data RTM have an imaged zone with the shape of a triangle whose apex is at the upper part of the fibre and the base is at the lower part. The explanation can be that in the synthetic experiments, forward and back propagated wavefields are exactly the same and this increases the correlation of events at the top of the section. On the other hand, in the real experiments the events only have significant correlations in the deeper part.

With respect to the techniques that transform strain rate to particle velocity, the three real VSP DAS migrations showed very similar characteristics. The main difference was an apparent change of polarity of the Daley technique with respect to the other two (8). Although untransformed data give an apparent similar response to the transformed data, a more detailed analysis is needed to check that the resulting images have a physical meaning.

When comparing the geophone RTM and the DAS RTM we found in Figure 8 that the main difference was the size of the imaged zone, but this is attributed to the receiver spread size that is shorter in the geophone data. We also found in Figure 10 that the main difference was the vertical resolution, that is less in the geophone data, but this is due to the different source wavelets.

Finally, we noticed a mismatch in the arrival times between real and modelled shots (Figure 5). We need to improve the velocity and density models, and also apply better static corrections to correct this travel time mismatch. In the RTM there is an asymmetry around the well that might be caused by these incorrect travel times.

CONCLUSIONS

The RTM of the walkaway VSP DAS data from the CaMI Field Research Station is possible with the current data quality. This RTM have similar quality than the RTM from geophone data so we hope it could be used to perform monitoring at this facility. There were no apparent differences between the three RTM approaches we tested but we think a more detailed analysis is still needed. The Laplacian operator, widely used to eliminate low frequency noise caused by the RTM algorithms, was not needed when real VSP data were migrated.

ACKNOWLEDGEMENTS

We thank the sponsors of CREWES for continued support. This work was funded by CREWES industrial sponsors, and NSERC (Natural Science and Engineering Research Council of Canada) through the grant CRDPJ 461179-13. This work was also funded in part thanks to the Canada First Research Excellence Fund.

REFERENCES

- Baysal, E., Kosloff, D. D., and Sherwood, J. W. C., 1983, Reverse time migration: *GEOPHYSICS*, **48**, No. 11, 1514–1524, <https://doi.org/10.1190/1.1441434>.
URL <https://doi.org/10.1190/1.1441434>
- Bóna, A., Dean, T., Correa, J., Pevzner, R., Tertyshnikov, K., and Zaanen, L., 2017, Amplitude and phase response of DAS receivers, *in* 79th EAGE Conference and Exhibition 2017, <http://earthdoc.eage.org/publication/publicationdetails/?publication=88917>.
- Chang, W., and McMechan, G. A., 1986, Reverse-time migration of offset vertical seismic profiling data using the excitation-time imaging condition: *GEOPHYSICS*, **51**, No. 1, 67–84, <https://doi.org/10.1190/1.1442041>.
- Chavarria, J. A., Kahn, D., Langton, D., Cole, S., and Li, X., 2019, Time-lapse waw vsp imaging of an unconventional reservoir using das fiber optics, *in* Unconventional Resources Technology Conference, Denver, Colorado, 22-24 July 2019, 1157–1165, <https://library.seg.org/doi/pdf/10.15530/urtec-2019-922>.
- Chon, Y., Souza, J., Planchart, C., and Lafourcade, P., 2003, Offset vsp imaging with elastic reverse time migration, *in* SEG Technical Program Expanded Abstracts 2003, 1079–1082, <https://library.seg.org/doi/pdf/10.1190/1.1817460>.
- Collino, F., and Tsogka, C., 2001, Application of the perfectly matched absorbing layer model to the linear elastodynamic problem in anisotropic heterogeneous media: *GEOPHYSICS*, **66**, No. 1, 294–307, <https://doi.org/10.1190/1.1444908>.
- Cosma, C., Balu, L., and Enescu, N., 2010, 3D VSP migration by image point transform: *GEOPHYSICS*, **75**, No. 3, S121–S130, <https://doi.org/10.1190/1.3396316>.
- Cosma, C., and Heikkinen, P., 1996, Seismic investigations for the final disposal of spent nuclear fuel in finland: *Journal of Applied Geophysics*, **35**, No. 2, 151 – 157, *recent Advances in Exploration Geophysics*, <http://www.sciencedirect.com/science/article/pii/092698519600016X>.
- Daley, T., Miller, D., Dodds, K., Cook, P., and Freifeld, B., 2016, Field testing of modular borehole monitoring with simultaneous distributed acoustic sensing and geophone vertical seismic profiles at Citronelle, Alabama: *Geophysical Prospecting*, **64**, No. 5, 1318–1334, <https://onlinelibrary.wiley.com/doi/pdf/10.1111/1365-2478.12324>.
- Daley, T. M., Freifeld, B. M., Ajo-Franklin, J., Dou, S., Pevzner, R., Shulakova, V., Kashikar, S., Miller, D. E., Goetz, J., Henniges, J., and Lueth, S., 2013, Field testing of fiber-optic distributed acoustic sensing (DAS) for subsurface seismic monitoring: *The Leading Edge*, **32**, No. 6, 699–706, <https://doi.org/10.1190/tle32060699.1>.
- Dillon, P. B., 1985, VSP migration using the Kirchhoff integral, *in* SEG Technical Program Expanded Abstracts 1985, 19–22, <https://library.seg.org/doi/pdf/10.1190/1.1892721>.
- Dillon, P. B., 1988, Vertical seismic profile migration using the Kirchhoff integral: *GEOPHYSICS*, **53**, No. 6, 786–799, <https://doi.org/10.1190/1.1442514>.
- Dillon, P. B., and Thomson, R. C., 1984, Offset source VSP surveys and their image reconstruction: *Geophysical Prospecting*, **32**, No. 5, 790–811, <https://onlinelibrary.wiley.com/doi/pdf/10.1111/j.1365-2478.1984.tb00739.x>.

- Gordon, A. J., 2019, Processing of DAS and geophone VSP data from the CaMI Field Research Station: M.Sc. thesis, University of Calgary, <https://prism.ucalgary.ca/handle/1880/110175?>
- Hartog, A. H., 2018, An introduction to distributed optical fibre sensors: CRC Press.
- He, R., Hornby, B., and Schuster, G., 2007, 3D wave-equation interferometric migration of VSP free-surface multiples: *GEOPHYSICS*, **72**, No. 5, S195–S203, <https://doi.org/10.1190/1.2743375>.
- Hou, A., Zhou, H., and Wiley, R. W., 2000, Reverse vsp prestack depth migration with multiples, in *SEG Technical Program Expanded Abstracts 2000*, 766–769, <https://library.seg.org/doi/pdf/10.1190/1.1816182>.
- Juškaitis, R., Mamedov, A. M., Potapov, V. T., and Shatalin, S. V., 1994, Interferometry with Rayleigh backscattering in a single-mode optical fiber: *Opt. Lett.*, **19**, No. 3, 225–227, <http://ol.osa.org/abstract.cfm?URI=ol-19-3-225>.
- Keho, T. H., 1984, Kirchhoff migration for vertical seismic profiles, in *SEG Technical Program Expanded Abstracts 1984*, 694–696, <https://library.seg.org/doi/pdf/10.1190/1.1894214>.
- Kwon, I. B., Kim, C. G., and Hong, C. S., 1999, A digital signal processing algorithm for structural strain measurement by a 3x3 passive demodulated fiber optic interferometric sensor: *Smart Materials and Structures*, **8**, No. 4, 433–440, <https://iopscience.iop.org/article/10.1088/0964-1726/8/4/301>.
- Lawton, D., Bertram, M., Hall, K., and Bertram, K., 2015, New approaches to seismic monitoring at the Brooks Field Research Station, Tech. rep., CREWES, <https://www.crewes.org/ForOurSponsors/ResearchReports/2015/CRR201541.pdf>.
- Lawton, D., Bertram, M., Saeedfar, A., Macquet, M., Hall, K., Bertram, K., Innanen, K., and Isaac, H., 2017, DAS and seismic installations at the CaMI Field Research Station, Newell County, Alberta, Tech. rep., CREWES, <https://www.crewes.org/ForOurSponsors/ResearchReports/2017/CRR201751.pdf>.
- Leung, V., Zhang, R., and Wong, M., 2013, Up- and down-going wave multiples rtm imaging for vsp, in *SEG Technical Program Expanded Abstracts 2013*, 5052–5056, <https://library.seg.org/doi/pdf/10.1190/segam2013-0631.1>.
- Liang, W., Wu, X., Wang, Y., and Yang, C., 2018, A simplified staggered-grid finite-difference scheme and its linear solution for the first-order acoustic wave-equation modeling: *Journal of Computational Physics*, **374**, 863 – 872, <http://www.sciencedirect.com/science/article/pii/S0021999118305333>.
- Liu, Y., Xue, H., and Zhang, L., 2018, Suppressing low-frequency and smearing artifacts of vsp reverse time migration using multidirectional wavefield decomposition, in *SEG 2018 Workshop: SEG Borehole Geophysics Workshop*, Guilin, China, 28-30 October 2018, 3–6, <https://library.seg.org/doi/pdf/10.1190/BHGP2018-02.1>.
- Lomas, A., satyan singh, and Curtis, A., 2019, Imaging vertical structures using Marchenko methods with vertical seismic profile data: *GEOPHYSICS*, **0**, No. ja, 1–46, <https://doi.org/10.1190/geo2018-0698.1>.
- Lou, M., Cheng, D., and Doherty, F., 2009, Suppressing vsp migration artifacts and noise by selected-aperture migration and damped-least-square smoothing, in *SEG Technical Program Expanded Abstracts 2009*, 4144–4148, <https://library.seg.org/doi/pdf/10.1190/1.3255737>.
- Lumley, D., Sherlock, D., Daley, T., Huang, L., Lawton, D., Masters, R., Verliac, M., and White, D., 2010, Highlights of the 2009 SEG Summer Research Workshop on CO2 sequestration: The Leading Edge, **29**, No. 2, 138–145, <https://doi.org/10.1190/tle29020138.1>.
- Macquet, M., and Lawton, D. C., 2017, Reservoir simulations and feasibility study for seismic monitoring at CaMI.FRS, Tech. rep., CREWES, <https://www.crewes.org/ForOurSponsors/ResearchReports/2017/CRR201756.pdf>.

- Macquet, M., Lawton, D. C., Saeedfar, A., and Osadetz, K. G., 2019, A feasibility study for detection thresholds of CO₂ at shallow depths at the CaMI Field Research Station, Newell County, Alberta, Canada: *Petroleum Geoscience*, **25**, No. 4, 509–518, <https://pg.lyellcollection.org/content/25/4/509.full.pdf>.
- Masoudi, A., Belal, M., and Newson, T. P., 2013, A distributed optical fibre dynamic strain sensor based on phase-OTDR: *Measurement Science and Technology*, **24**, No. 8, 085,204, <https://iopscience.iop.org/article/10.1088/0957-0233/24/8/085204>.
- Ranganayaki, R. P., and Moeckel, G. P., 1987, VSP migration: Synthetic and field examples, *in* SEG Technical Program Expanded Abstracts 1987, 777–781, <https://library.seg.org/doi/pdf/10.1190/1.1891960>.
- Sirkis, J. S., and Henry W. Haslach, J., 1991, Complete phase-strain model for structurally embedded interferometric optical fiber sensors: *Journal of Intelligent Material Systems and Structures*, **2**, No. 1, 3–24, <https://doi.org/10.1177/1045389X9100200101>.
- Wang, Y., Huang, L., and Zhang, Z., 2011, Reverse-time migration of time-lapse walkaway vsp data for monitoring co₂ injection at the sacroc eor field, *in* SEG Technical Program Expanded Abstracts 2011, 4304–4308, <https://library.seg.org/doi/pdf/10.1190/1.3628107>.
- Whitmore, N. D., and Lines, L. R., 1986, Vertical seismic profiling depth migration of a salt dome flank: *GEOPHYSICS*, **51**, No. 5, 1087–1109, <https://doi.org/10.1190/1.1442164>.
- Wiggins, W., Ng, P., and Manzur, A., 1986, The relation between the VSP-CDP transformation and VSP migration, *in* SEG Technical Program Expanded Abstracts 1986, 565–568, <https://library.seg.org/doi/pdf/10.1190/1.1892996>.
- Xue, H., and Liu, Y., 2017, Vsp reverse time migration based on complex wavefield decomposition, *in* SEG 2017 Workshop: Carbonate Reservoir E&P Workshop, Chengdu, China, 22-24 October 2017, 152–155, <https://library.seg.org/doi/pdf/10.1190/carbonate2017-42>.
- Yu, J., and Schuster, G. T., 2004, Enhancing illumination coverage of vsp data by crosscorrelogram migration, *in* SEG Technical Program Expanded Abstracts 2004, 2501–2504, <https://library.seg.org/doi/pdf/10.1190/1.1845235>.
- Zhao, X., and Jin, S., 2015, Vertical seismic profile Kirchhoff migration with structure dip constraint: *Interpretation*, **3**, No. 3, SW51–SW56, <https://doi.org/10.1190/INT-2014-0240.1>.